

Nonparabolic dispersion of charge carriers in CsPbI_3 in the orthorhombic phase.

O. S. Sultanov,^{1,2} D. K. Loginov,¹ I. V. Ignatiev,^{1,2} D. V. Pankin,³ M. B. Smirnov,² and M. S. Kuznetsova¹

¹*Spin Optics Laboratory, St. Petersburg State University,
Ulyanovskaya 1, Peterhof, St. Petersburg, 198504, Russia*

²*Faculty of Physics, St. Petersburg State University,
Ulyanovskaya 1, Peterhof, St. Petersburg, 198504, Russia*

³*Center for Optical and Laser Materials Research,
St. Petersburg State University, Ulyanovskaya 5, St. Petersburg 198504, Russia*

The dispersion curves for the electrons and holes in CsPbI_3 in the orthorhombic phase are calculated using the density functional theory (DFT), with the spin-orbit coupling taken into account. The effective masses of the charge carriers are obtained using the parabolic approximation of the dispersion curves in different directions in the k -space. It is found that the dispersion curves demonstrate strong nonparabolicity at energies above 0.2 eV for electrons and above 0.1 eV for holes, available for experimental study by the means of optical spectroscopy. We propose a model that describes the dispersion dependences of charge carriers at those energies, where the effective masses of the quasiparticles depend quadratically on the wave vector. An expression is obtained according to the model, which can accurately approximate the dispersion curves for the electron and the hole in all symmetric directions from the center to the boundary of the Brillouin zone.

I. INTRODUCTION

The optical materials based on lead halide perovskite nanocrystals are promising due to their unique optical [1–5], optoelectronic [6–13], and photovoltaic [12, 14–18] properties. The study of CsPbX_3 (X= Cl, Br, I) perovskite nanocrystals (NCs) is a highly challenging problem in optical materials science. Particularly, prospects of application of the CsPbX_3 -based NCs have been demonstrated for lasers [19], polarizers [20], light-emitting diodes [6, 8, 21, 22], solar cells [14, 16–18, 23–26], and photodetectors [27]. The knowledge of fundamental properties of these materials is important for the design of practical devices.

The electronic energy band structure is one of particular importance in this regard and can be studied both experimentally and theoretically [28–30]. Experimentally, it has been studied for perovskite NCs through various optical methods, such as the measurement of photoluminescence (PL) and the photoluminescence excitation spectra (PLE) [30, 31]. In particular, those methods allow for the observation of not only the ground states of charge carriers (electrons and holes), but also the quantum-confined excited states in various nanostructures. This enables the experimental study of dispersion dependences in the valence and conduction bands. The experimental results show [32] that it is possible to resolve quantum-confined states with energies of a fraction of an electron-volt.

However, these experimental studies should be supported by theoretical analysis. The relevance of such theoretical studies is due to the fact that the commonly used effective mass model no longer holds at those energies, and the dispersion curves assume a non-parabolic shape [33–35]. Additionally, no comprehensive theory describing the nonparabolicity of the charge carrier dispersion in perovskites has been proposed so far, despite the importance of the effect on the optical properties of

the material.

This paper is dedicated to the development of the theoretical model that describes the nonparabolic dispersion of the charge carriers in lead halide perovskites. We propose an approach based on the DFT calculation of the electronic band structure of CsPbI_3 in the orthorhombic phase [28, 30, 36–42]. The data obtained from this calculation is used to determine the energy range in which the effective mass model for the charge carriers is applicable. Then, a novel theoretical model is constructed using the results of the DFT calculation that can describe the dispersion dependences of the electrons and the holes with greater precision in a greater range of energies compared to the effective mass model.

II. SIMULATION OF THE CRYSTAL BAND STRUCTURE OF CsPbI_3

It has been shown [42] that CsPbI_3 has an orthorhombic structure at low temperatures, with the respective phase known as γ - CsPbI_3 . The respective unit cell, as well as the first Brillouin zone(BZ), is schematically shown in Fig. 1. The unit cell contains four formula units of CsPbI_3 . The coordinates of the high symmetry points are given in Tab. I. The wave vector components, k_x , k_y , and k_z , are measured in units proportional to the inverse lattice constants, a_x , a_y , and a_z , respectively.

In order to perform the calculation of the energy band structure, the generalized gradient approximation (GGA) of density functional theory (DFT) with the Perdew-Burke-Ernzerhoff (PBE) functional is chosen [37]. The Tkatchenko-Scheffler (TS) approach is used to take the dispersion corrections [38] into account. The spin-orbit coupling (SOC) is taken into consideration. The norm-conserving pseudopotentials [37] and the plane wave basis set with a 1200 eV cutoff energy are used. The self-consistent field convergence criterion

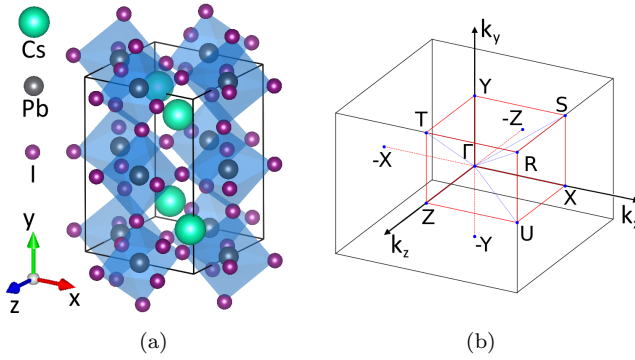


FIG. 1: (a) The unit cell of the orthorhombic CsPbI_3 crystal lattice [43, 44]. The image of the unit cell is taken from the Materials Project for CsPbI_3 (mp-1120768) from database version v2025.09.25. The lattice constants obtained from the DFT calculation are $a_x = 0.907$ nm, $a_y = 1.254$ nm, and $a_z = 0.801$ nm. The values of the constants agree well with those obtained via X-ray diffraction in [42]. (b) The first BZ with the primitive reciprocal lattice vectors, $b_\alpha = 1/a_\alpha$, where $\alpha = x, y, z$. The labels Γ , X, Y, etc. show the high-symmetry points used in the DFT calculations.

TABLE I: The relative coordinates of the high symmetry points in the first Brillouin zone, in units of the vectors of the reciprocal lattice, are $2\pi/a_x = 6.93$ nm $^{-1}$, $2\pi/a_y = 5.01$ nm $^{-1}$, and $2\pi/a_z = 7.84$ nm $^{-1}$.

Point	$k_x, \frac{2\pi}{a_x}$	$k_y, \frac{2\pi}{a_y}$	$k_z, \frac{2\pi}{a_z}$
Z	0.0	0.0	0.5
T	0.0	0.5	0.5
Y	0.0	0.5	0.0
S	0.5	0.5	0.0
X	0.5	0.0	0.0
U	0.5	0.0	0.5
R	0.5	0.5	0.5

is 10^{-7} eV/atom. The calculations are performed in CASTEP software [37, 39].

At the initial stage, the crystal geometry optimization was performed using the modified Broyden-Fletcher-Goldfarb-Schanno (LBFGS) approach [40, 41] until the residual forces, residual stresses, and maximum displacements were smaller than 0.01 eV/Å, 0.02 GPa, and 5×10^{-4} Å, respectively. In the reciprocal space, the Monkhorst-Pack grid of points was used with the \mathbf{k} -vector step equal to 0.04 1/Å [45]. The band structure calculations were performed within the 10 eV energy range with a 0.96 eV scissor operator and a 0.006 1/Å separation. The electron energy states are calculated for many points in the Brillouin zone to accurately reproduce the dispersion curves for charge carriers.

The energy structure of the orthorhombic CsPbI_3 crystal calculated via the DFT method is shown in Fig. 2.

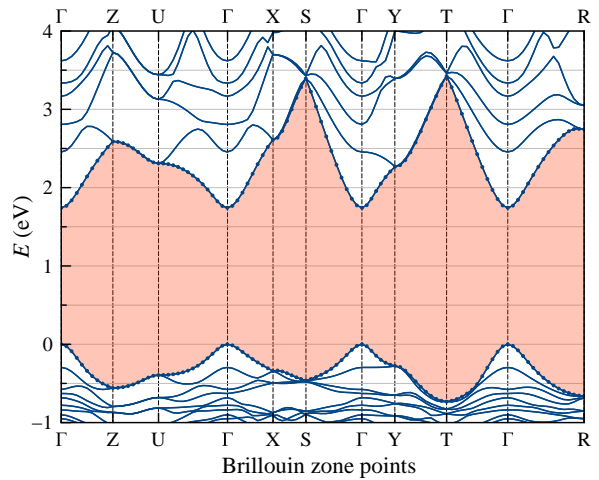


FIG. 2: The dispersion dependences for the valence and the conduction bands in γ - CsPbI_3 is calculated via the DFT method, with the spin-orbit coupling taken into account.

The figure shows the dispersion dependences, $E(\vec{k})$, for the electrons in multiple conduction subbands and for the holes in multiple valence subbands. Note that the narrowest band gap of the orthorhombic CsPbI_3 crystal is at the Γ -point.

As seen in Fig. 2, the dispersion curves of different subbands approach each other and become degenerate at critical points of the Brillouin zone. Moreover, some of the dispersion curves undergo anti-crossings and are split due to their interaction. Similar behavior is observed for both the valence and the conduction subbands. The DFT calculations yield the model-accurate dispersion curves, which, however, are difficult to analyze. Therefore, we provide a simple explanation of the behavior of those curves based on the $\mathbf{k} \cdot \mathbf{p}$ approach described, see, e.g., Ref. [46]. The $\mathbf{k} \cdot \mathbf{p}$ method is based on the consideration of the local behavior of the dispersion dependences within the framework of perturbation theory. The coupling of the valence and conduction subbands is described within this approach by operators of the form:

$$V = \frac{\hbar}{2m_0} k_\alpha p_{n,m}^{(\alpha)}. \quad (1)$$

Here k_α is the wave vector of an electron in the conduction band or a hole in the valence band, where $\alpha = x, y, z$ are the coordinates of the electron and hole within the unit cell of the crystal, and m_0 is the free electron mass. The matrix elements $p_{n,m}$ take the form $p_{n,m}^{(\alpha)} = \langle u_n | \hat{p}_\alpha | u_m \rangle$, where the operator $\hat{p}_\alpha = -i\hbar\partial/\partial\alpha$ is the electron or hole momentum. The quantities $u_{n(m)}$ are the Bloch amplitudes of the electron or the hole wave functions, and indices n, m determine the spin and orbital angular momentum of electrons or holes in conduction and valence bands, respectively.

The dispersion dependences in the vicinity of the Γ

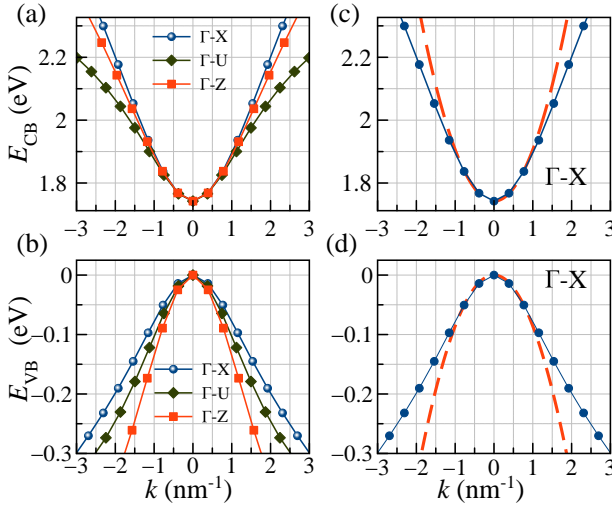


FIG. 3: The dispersion curves in the Γ -X, Γ -Z, and Γ -U directions for electrons (a) and holes (b). The dispersion curves for the electrons (c) and the holes (d) in the Γ -X direction are provided as an example. The points show the dispersion curves obtained from the DFT calculation; the dashed line shows the effective mass approximation (see Eq. (1)).

point are of particular importance for the analysis of optical transitions near the band gap. The dispersion curves are mainly determined by the coupling of the topmost valence subband with the lowest conduction subband. This coupling is described by the matrix element of the operator (1) and provides the main contribution to the effective masses of the electron and the hole near the Γ point. In the vicinity of the Γ -point, the energies of electrons and holes can be calculated in the framework of the $\mathbf{k} \cdot \mathbf{p}$ method using perturbation theory. This approach yields a parabolic dependence of the energies of both electrons and holes. This behavior is readily interpreted as the kinetic energy of free charge carriers with some effective mass m^* .

The coupling of different subbands within the conduction or valence band can also contribute to the effective masses of the electron and hole. However, an analysis shows that this contribution is small for the nearest subbands in the vicinity of the Γ point. The interaction of subbands becomes valuable for the critical points near the surface of the Brillouin zone. Such interactions contribute to the nonparabolicity of the dispersion dependences at large wave vectors.

The dispersion dependences for the Γ -X, Γ -Z, and Γ -U directions are shown in Fig. 3. The anisotropy (corrugation effect) and nonparabolicity of the curves are clearly seen here. The data obtained from the DFT calculations can be used to calculate the effective masses of the charge carriers.

III. THE APPLICABILITY OF THE EFFECTIVE MASS APPROXIMATION

Let us discuss the dispersion dependences using the effective mass model for the electron in the lower conduction subband and the hole in the upper valence subband, as well as estimate the energy range in which the model is applicable.

The dispersion dependences in a given direction in reciprocal space can be approximated, in the general case, by a polynomial of the wave vector. In semiconductors with a degenerate valence band, or in narrow-gap materials, the dispersion of charge carriers can be nonparabolic in the vicinity of the Γ -point [47–49]. In lead-halide perovskites such as CsPbI_3 , the band gap is wide enough, and both the lower conduction subband and the upper valence subband are only spin-degenerate. Therefore, for small enough values of k , we can use a single quadratic term of the polynomial that is the effective mass approximation

$$H(\vec{k}) \approx Ak_\alpha^2 = \frac{\hbar^2}{2m_\alpha^*} k_\alpha^2. \quad (2)$$

Here H is the total energy of the quasiparticle, k_α is the wave vector, $\alpha = x, y, z$, and m_α^* is the effective mass of the electron or the hole that depends on the direction of the wave vector. The expression for the inverse effective masses of the electron and hole in Eq. (2) can be obtained within the $\mathbf{k} \cdot \mathbf{p}$ method in the second-order perturbation theory of the operator given in Eq. (1), see, e.g., Ref. [46]. As mentioned above, the values of the effective mass are determined by the coupling of the top valence subband and the bottom conduction subband.

The orthorhombic phase of CsPbI_3 exhibits significant anisotropy of dispersion dependencies, as demonstrated in Figs. 3 (a) and (b) for the directions Γ -X, Γ -Z, and Γ -U in the Brillouin zone. Figure 3 (c) and (d) shows an example of the parabolic approximation of dispersion curves at small k values. As seen, the approximation well describes the dispersion curve in a small energy range, 0.1 eV for the valence band and 0.2 eV for the conduction band.

The effective masses of the charge carriers obtained from the least-squares fitting of the dispersion curves in all the studied directions, as well as the average effective mass, are given in Tab. II. The fit interval has been chosen as $[-0.5, 0.5] \text{ nm}^{-1}$ for the Γ -Y and Γ -U directions and $[-1, 1] \text{ nm}^{-1}$ for the other directions. The average effective masses, \tilde{m}_e^* and \tilde{m}_h^* , are given by

$$\frac{1}{\tilde{m}_e^*} = \frac{1}{N} \sum_{i=1}^N \frac{1}{m_{e,i}^*} \quad (3)$$

where i enumerates different directions in the reciprocal space, and $m_{e,i}^*$ is the effective mass of the electron in the corresponding direction. A similar expression should be used for the average effective mass of holes. Using

these values, we have also calculated the reduced exciton effective mass

$$\frac{1}{\mu_X} = \frac{1}{m_e^*} + \frac{1}{m_h^*} \quad (4)$$

TABLE II: The effective masses of electrons m_e^* and holes m_h^* (in units of free electron mass, m_0) in different directions in reciprocal space are obtained from the parabolic approximation of the dispersion curves.

	Γ –Z	Γ –T	Γ –Y	Γ –S	Γ –X	Γ –U	Γ –R	Average
m_h^*	0.23	0.26	0.17	0.37	0.45	0.33	0.33	0.27
m_e^*	0.25	0.24	0.15	0.23	0.23	0.29	0.25	0.23
μ_X	0.12	0.12	0.08	0.14	0.15	0.15	0.14	0.13

The values that have been obtained for the average effective masses are in good agreement with the results obtained for orthorhombic CsPbI_3 in [42] using the GW method (0.23 m_0 for electrons and 0.24 m_0 for holes). The values of the reduced exciton effective masses are also in good agreement with those obtained from, e.g., Ref. [42].

IV. THE ANALYSIS OF NON-PARABOLIC DISPERSION AND THE CORRUGATION EFFECT

The parabolic approximation presented above is applicable when the bottom conduction subband and the top valence subband are non-degenerate and strongly separate from the other conduction and valence subbands, respectively. Accordingly, their interaction can be neglected at sufficiently small \vec{k} values. As shown in Fig. 3(c, d), the parabolic approximation is no longer applicable at energies of about 0.1 eV (in absolute value) for holes and 0.2 eV for electrons, and a more complex model should be applied to describe the dispersion dependences. This means that the perturbation theory used in the $\mathbf{k} \cdot \mathbf{p}$ method is no longer correct for large wave vectors. The reason for that is the relatively large kinetic energy of the charge carrier motion, which becomes comparable to the energy separation between the sub-bands in the conduction and valence bands (see Fig. 2). In this case, the nonparabolicity of electron (hole) dispersion is due to the coupling between the lowest conduction (upper valence) subband and the other conduction (valence) subbands.

Figure 2 shows that, when the upper and lower conduction subbands approach the high-symmetry points of the Brillouin zone surface, they become degenerate. The upper valence subbands exhibit similar behavior. The convergence of the subbands is accompanied by an increase in the degree of nonparabolicity. This behavior can, in principle, be described using the $\mathbf{k} \cdot \mathbf{p}$ method near the respective point of the Brillouin zone. However, in our case, more precise results are given by the DFT calculations.

Here, we propose a model that allows one to describe the dispersion dependences in a large range of wave vectors up to the Brillouin zone boundary. The model is based on a phenomenological formula for the kinetic energy of a quasiparticle with an effective mass, which is parametrically dependent on the wave vector:

$$H(\vec{k}) = \frac{\hbar^2}{2} \sum_{\alpha=1}^3 \frac{1}{m_{\alpha}^*(\vec{k})} k_{\alpha}^2 \quad (5)$$

where $\alpha = x, y, z$, and the effective masses in different directions $m_{\alpha}^*(\vec{k})$ depend on the wave vector \vec{k} . We propose the following model for the k -dependent effective mass:

$$m_{\alpha}^*(\vec{k}) = m_{\alpha}^*(0) \left(1 + \sum_{\beta} \sum_{\gamma} B_{\beta\gamma} |k_{\beta} k_{\gamma}| \right). \quad (6)$$

Here the indices $\alpha, \beta, \gamma = x, y, z$. The quantities $m_{\alpha}^*(0)$ are the components of the effective mass tensor given in Eq. (2), and $B_{\beta\gamma}$ are the elements of a 3x3 symmetric matrix \mathbb{B} of real-valued coefficients. The matrix \mathbb{B} is an effective tensor that describes the strength of the interaction between the bottom conduction subband for electrons (or the top valence sub-band for holes) and the other electron and hole subbands, respectively. As shown in Fig. 4, this approximation allows one to describe the dispersion curves with significantly better precision (the mean-square error is $4.3 \cdot 10^{-4}$ eV for electrons and $6.5 \cdot 10^{-5}$ eV for holes) in a larger energy range, up to 0.5 eV above the bottom of the conduction band and up to 0.25 eV below the top of the valence band. The coefficients of the approximation obtained for the different directions in reciprocal space are provided in Tab. III. The approximations for the other directions in the Brillouin zone are given in Appendix A. It should be emphasized that only 9 model parameters were sufficient to describe the dispersion in the 7 symmetrical directions of the Brillouin zone.

We can also determine the effective mass for all other symmetric directions in the Brillouin zone, for example, for the Γ –U direction $k_x = \sqrt{a_x^2 + a_z^2} k/a_x$, $k_y = 0$, $k_z = \sqrt{a_x^2 + a_z^2} k/a_z$, and Eq. (5) and (6) yield

$$H(\vec{k}) = \frac{\hbar^2}{2} (a_x^2 + a_z^2) \left(\frac{1}{a_x^2 m_x^*(\vec{k})} + \frac{1}{a_z^2 m_z^*(\vec{k})} \right) k^2 \quad (7)$$

$$\equiv \frac{\hbar^2 k^2}{2 m_{\text{U}}^*(\vec{k})},$$

where a_x , a_y , and a_z are the lattice constants, the values of which are given in the caption to Fig. 1. It follows from this expression that the unversed effective mass in the Γ –U direction is calculated as

$$\frac{1}{m_{\text{U}}^*(\vec{k})} = (a_x^2 + a_z^2) \left(\frac{1}{a_x^2 m_x^*(\vec{k})} + \frac{1}{a_z^2 m_z^*(\vec{k})} \right). \quad (8)$$

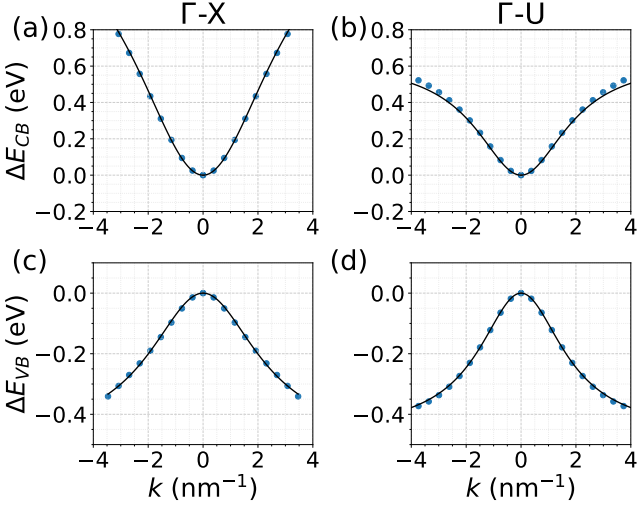


FIG. 4: Examples of the dispersion curves for electrons (a,b) and holes (c,d) in directions Γ –X (a,c) and Γ –U (b,d) in the Brillouin zone, fitted using the nonparabolic model (see Eqs. (5) and (6)). The dots represent the DFT data, and the solid curves correspond to the least-squares fit of the data to the model.

Similar expressions are valued for other directions, Γ –S and Γ –T. For the Γ –R direction, the expression for the inverse effective mass is a bit more complex

$$\frac{1}{m_R^*(\vec{k})} = (a_x^2 + a_y^2 + a_z^2) \cdot \left(\frac{1}{a_x^2 m_x^*(\vec{k})} + \frac{1}{a_y^2 m_y^*(\vec{k})} + \frac{1}{a_z^2 m_z^*(\vec{k})} \right). \quad (9)$$

TABLE III: The nonparabolic dispersion coefficients in Eq. (5) for the electrons and the holes in reciprocal space were obtained from the least-squares fit of the data obtained from the DFT calculation. m_α^* are given in units of free electron mass, and $B_{\beta\gamma}$ are given in nm².

Coefficient	Electrons		Holes	
	Value	Error	Value	Error
$m_x^*(0)$	0.233	$0.8 \cdot 10^{-3}$	0.452	$9.7 \cdot 10^{-3}$
$m_y^*(0)$	0.150	$2.0 \cdot 10^{-3}$	0.173	$1.8 \cdot 10^{-3}$
$m_z^*(0)$	0.254	$3.1 \cdot 10^{-3}$	0.227	$2.0 \cdot 10^{-3}$
B_{xx}	0.103	$0.9 \cdot 10^{-5}$	0.170	$1.4 \cdot 10^{-5}$
B_{yy}	0.300	$12.0 \cdot 10^{-5}$	0.639	$14.0 \cdot 10^{-5}$
B_{zz}	0.111	$0.7 \cdot 10^{-5}$	0.235	$0.6 \cdot 10^{-5}$
B_{xy}	-0.217	$7.4 \cdot 10^{-5}$	-0.211	$7.3 \cdot 10^{-5}$
B_{yz}	-0.223	$6.0 \cdot 10^{-5}$	-0.347	$5.9 \cdot 10^{-5}$
B_{zx}	0.280	$3.4 \cdot 10^{-5}$	0.159	$3.0 \cdot 10^{-5}$

The phenomenological model based on Eqs. (5) and (6) has no strict mathematical justification. One can

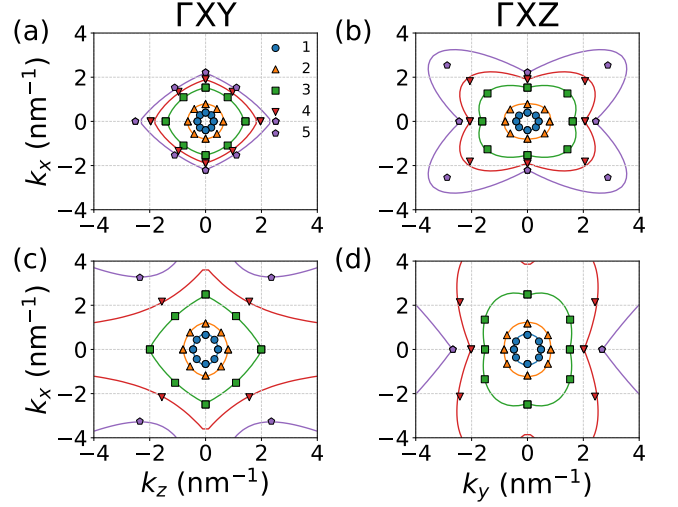


FIG. 5: The cross-sections for energy isosurfaces for electron (top) and hole (bottom) in the Γ XZ (a,c) and the Γ XY (b,d) planes. Symbols are the DFT calculations. Solid lines are the modeling using Eqs. (5), (6), and values of parameters listed in Tab. III. The cross-section energies are $\Delta E_{e,1} = 0.03$ eV; $\Delta E_{e,2} = 0.10$ eV; $\Delta E_{e,3} = 0.31$ eV; $\Delta E_{e,4} = 0.43$ eV; $\Delta E_{e,5} = 0.53$ eV for electrons, and $\Delta E_{h,1} = -0.04$ eV; $\Delta E_{h,2} = -0.10$ eV; $\Delta E_{h,3} = -0.25$ eV; $\Delta E_{h,4} = -0.35$ eV; $\Delta E_{h,5} = -0.45$ eV for holes.

only assume that the strong nonparabolicity of the dispersion curves indicates a sufficiently strong coupling of various subbands. This cannot be described within the framework of the low-order perturbation theory used in the $\mathbf{k} \cdot \mathbf{p}$ method to justify the effective mass model. Similar problems related to the strong interaction of particles are discussed in other branches of physics (for example, quantum electrodynamics), where appropriate theoretical approaches have been developed, see Ref. [50].

The model based on Eqs. (5) and (6) can be useful for theoretical modeling of the quantum-confined states of electrons and holes in various nanocrystals. Usage of analytical expressions (5) and (6) for the Hamiltonian of the quantum problem, rather than the numerical DFT results, allows one to formulate and solve the problem in a traditional way. We will discuss the problem elsewhere.

In addition to strong nonparabolicity, the problem of the quantum-confined states is complicated by a strong corrugation effect, that is, the dependence of the dispersion curve parameters on the wave vector direction in the reciprocal space, as it is already illustrated in Fig. (3) and Tabs. II and III. To visualize the corrugation effect more clearly, we present in Fig. (5) the curves of constant energy in different planes in the reciprocal space for the charge carriers. These curves are the cross-section of the energy isosurfaces of the electron and the hole.

As is evident, the curves of constant energy are circles or weakly elongated ellipses at small wave vectors and,

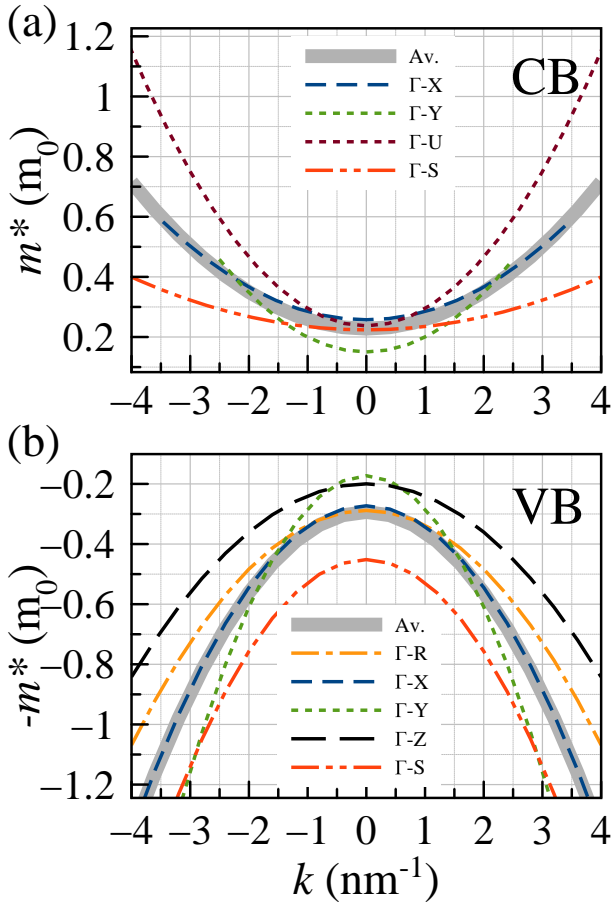


FIG. 6: Colored curves are the effective masses of electrons (a) and holes (b) in different directions in the Brillouin zone. Solid grey curves are the average effective mass derived using Eq. (10). The effective mass values for the hole are provided as negative values for posterity.

respectively, at a small energy shift, ΔE , from the bottom (top) of the conduction (valence) band. This is the area in k space where the parabolic fit of the dispersion curves is a good approximation, see Fig. 3(b).

The curves of constant energy diverge from the elliptic-like shape at larger wave vectors and larger ΔE . For example, the curve of constant energy has a more complex shape for $\Delta E_{e,5} = 0.53$ eV, see Fig. 5 (c). In the valence band, they are significantly elongated along the k_x direction. This corrugation of the conduction and valence bands should affect the energy states of carriers and, in particular, split the states that are degenerate with respect to the angular momentum.

For the solution of the quantum-confined state problem in the nanocrystals, which size is considerably larger than the lattice constant, an envelope wave function approximation can be employed. In this case the effective mass of a charge carrier parametrically dependent on the carrier wave vector is also a good approximation. Using

Eq. (6) and Tab. III, we have calculated the electron and hole masses as functions of wave vectors in different directions. They are shown in Fig. 6. The anisotropy, as well as a significant increase in the effective mass with the increase of the wave vector, is evident.

In addition, we have calculated the averaged electron and hole effective masses as functions of wave vectors. They are frequently used for simplified calculations of the quantum-confined states [32]. The averaged effective masses are useful for the calculation of the wave functions corresponding to the ground states of the electron and the hole having the highest possible symmetry. We can assume that the charge carrier cloud in the lowest energy state (the s-like state) averages the structure properties in different directions, thus diminishing the corrugation effect.

We introduce the average effective mass as

$$\frac{1}{\tilde{m}^*}(|\vec{k}|) = \int_0^\pi \sin \theta d\theta \int_0^{2\pi} d\varphi \frac{1}{m_i^*(\vec{k})} \quad (10)$$

where $m_i^*(\vec{k})$ is the effective mass of the electron or the hole, $|\vec{k}|$ is the absolute value of the wave vector \vec{k} , and θ and φ are the angles in spherical coordinates,

$$\begin{cases} k_x = |\vec{k}| \sin \theta \cos \varphi \\ k_y = |\vec{k}| \sin \theta \sin \varphi \\ k_z = |\vec{k}| \cos \theta \end{cases} \quad (11)$$

where $\vec{k} = (k_x, k_y, k_z)^T$. The average effective mass introduced in this way can then be used to estimate the degree of anisotropy in the system.

As can be seen, the electron effective masses are greater than the average mass in the Γ -U direction. In both the Γ -X and Γ -Z directions, the electron effective masses are approximately the same as their average electron mass. In the Γ -T direction, the electron effective mass is smaller than the average one.

At the same time, the absolute value of the effective mass of the hole in the Γ -T direction is greater than its average hole mass. The absolute values of the hole masses in the Γ -U and Γ -Z directions are greater than the average value.

It should be noted that the averaged reduced mass can be used to analyze the energy of charge carriers in spherical nanocrystals of γ -CsPbI₃. The spherical shape of the nanocrystals imposes spherically symmetric boundary conditions on the anisotropic crystal structure of the perovskite. Therefore, the energy of the transition between the upper hole and the lower electron energy levels of size quantization can be described using the average inverse effective mass (Eq. (10)).

V. CONCLUSION

A comprehensive DFT calculation of the energy band structure in the γ -CsPbI₃ orthorhombic perovskite accounting for the spin-orbit interaction is performed. It is

established that at sufficiently large wave vectors, the dispersion dependences of charge carriers in both the lower conduction subband and the upper valence subband are strongly nonparabolic. The effective mass approximation only holds for the absolute values of energy up to 0.1 eV for holes and 0.2 eV for electrons with respect to the edge of the band gap. Additionally a significant corrugation effect has been observed.

A phenomenological model is proposed that describes the dispersion dependences of charge carriers in a large range of wave vectors. It is found that the dispersion in the 7 symmetric directions in the Brillouin zone can be described by the nine-parametric model. The effective mass is found to quadratically depend on the wave vector within this model. As such, the model can accurately describe the nonparabolicity of the dispersion, as well as the corrugation effect for the charge carriers in perovskites.

We believe that the proposed phenomenological model is not specific for the crystal under study and can be applied to the description of dispersion dependences of charged carriers in other crystals. The proposed model with the k -dependent effective mass is able to describe dispersion curves in a much larger wave vector range, up to the anticrossing point with other subbands, than the model with the constant effective mass. The model is useful for the analysis of optical spectra of the perovskite nanocrystals, which are small enough to observe the highly excited states of electrons and holes lying in the energy range of the substantial nonparabolicity of dispersion.

VI. ACKNOWLEDGEMENT

The authors acknowledge the Saint-Petersburg University for the Research Grant No. 125022803069-4.

Appendix A: The dispersion curves of charge carriers

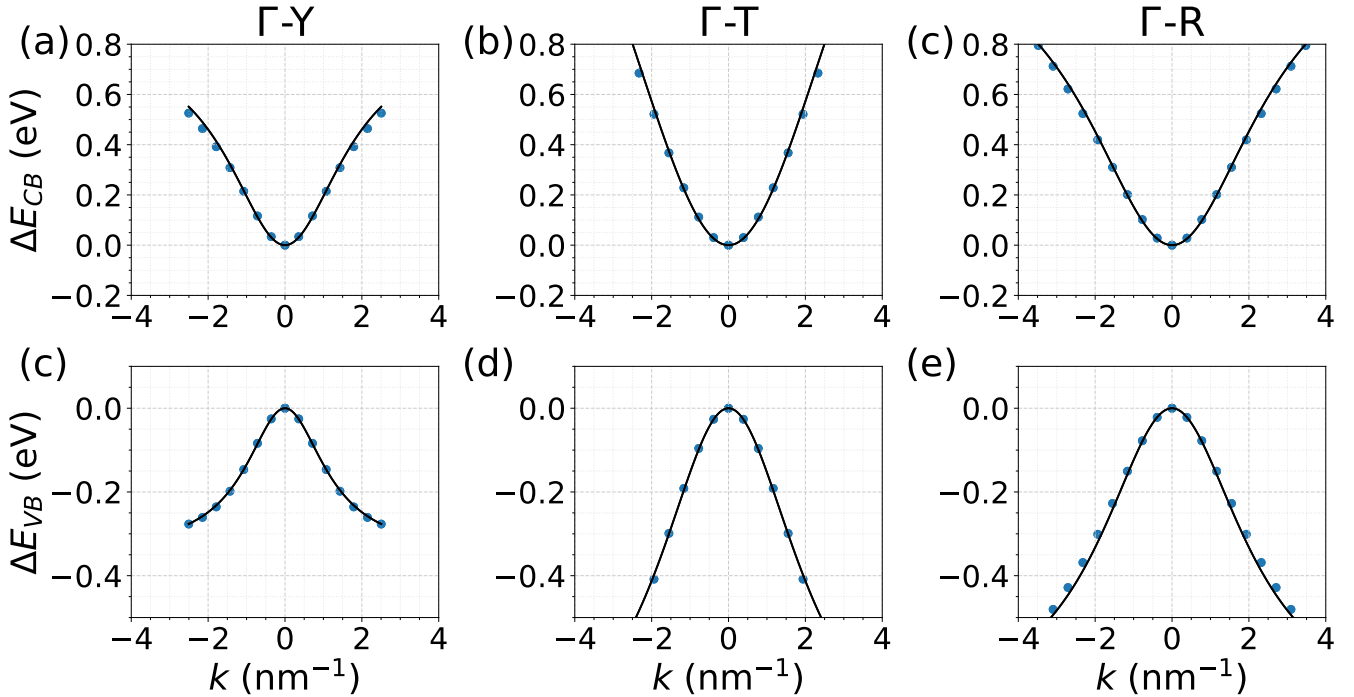


FIG. 7: The dispersion curves of electrons (top) and holes (bottom) in the Γ -Y, Γ -T, and Γ -R directions, approximated by Eqs. (5) and (6) with parameters listed in Tab. III

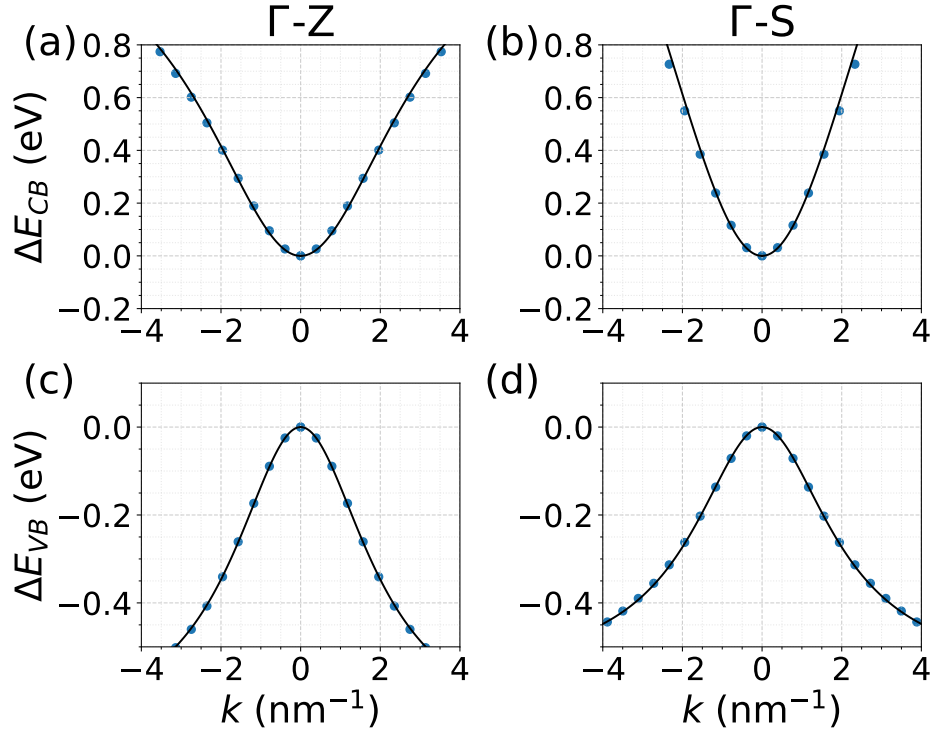


FIG. 8: The dispersion curves of electrons (top) and holes (bottom) in the Γ -Z and Γ -S directions, , approximated by Eqs. (5) and (6) with parameters listed in Tab. III.

[1] X. Li, Y. Wu, S. Zhang, B. Cai, Y. Gu, J. Song, and H. Zeng, “CsPbX₃ Quantum Dots for Lighting and Displays: Room-Temperature Synthesis, Photoluminescence Superiorities, Underlying Origins and White Light-Emitting Diodes,” *Adv Funct Materials*, vol. 26, pp. 2435–2445, Apr. 2016. Publisher: Wiley.

[2] S. Yakunin, L. Protesescu, F. Krieg, M. I. Bodnarchuk, G. Nedelcu, M. Humer, G. De Luca, M. Fiebig, W. Heiss, and M. V. Kovalenko, “Low-threshold amplified spontaneous emission and lasing from colloidal nanocrystals of caesium lead halide perovskites,” *Nat Commun*, vol. 6, Aug. 2015. Publisher: Springer Science and Business Media LLC.

[3] P. Ramasamy, D.-H. Lim, B. Kim, S.-H. Lee, M.-S. Lee, and J.-S. Lee, “All-inorganic cesium lead halide perovskite nanocrystals for photodetector applications,” *Chem. Commun.*, vol. 52, no. 10, pp. 2067–2070, 2016. Publisher: Royal Society of Chemistry (RSC).

[4] Q. A. Akkerman, G. Rainò, M. V. Kovalenko, and L. Manna, “Genesis, challenges and opportunities for colloidal lead halide perovskite nanocrystals,” *Nature Mater*, vol. 17, pp. 394–405, May 2018. Publisher: Springer Science and Business Media LLC.

[5] G. Nedelcu, L. Protesescu, S. Yakunin, M. I. Bodnarchuk, M. J. Grotevent, and M. V. Kovalenko, “Fast Anion-Exchange in Highly Luminescent Nanocrystals of Cesium Lead Halide Perovskites (CsPbX₃, X = Cl, Br, I),” *Nano Lett.*, vol. 15, pp. 5635–5640, Aug. 2015. Publisher: American Chemical Society (ACS).

[6] Z.-K. Tan, R. S. Moghaddam, M. L. Lai, P. Docampo, R. Higler, F. Deschler, M. Price, A. Sadhanala, L. M. Pazos, D. Credgington, F. Hanusch, T. Bein, H. J. Snaith, and R. H. Friend, “Bright light-emitting diodes based on organometal halide perovskite,” *Nature Nanotech*, vol. 9, pp. 687–692, Sept. 2014. Publisher: Springer Science and Business Media LLC.

[7] L. Protesescu, S. Yakunin, M. I. Bodnarchuk, F. Krieg, R. Caputo, C. H. Hendon, R. X. Yang, A. Walsh, and M. V. Kovalenko, “Nanocrystals of Cesium Lead Halide Perovskites (CsPbX₃, X = Cl, Br, and I): Novel Optoelectronic Materials Showing Bright Emission with Wide Color Gamut,” *Nano Lett.*, vol. 15, pp. 3692–3696, June 2015. Publisher: American Chemical Society.

[8] H. Cho, S.-H. Jeong, M.-H. Park, Y.-H. Kim, C. Wolf, C.-L. Lee, J. H. Heo, A. Sadhanala, N. Myoung, S. Yoo, S. H. Im, R. H. Friend, and T.-W. Lee, “Overcoming the electroluminescence efficiency limitations of perovskite light-emitting diodes,” *Science*, vol. 350, pp. 1222–1225, Dec. 2015. Publisher: American Association for the Advancement of Science (AAAS).

[9] M. V. Kovalenko, L. Protesescu, and M. I. Bodnarchuk, "Properties and potential optoelectronic applications of lead halide perovskite nanocrystals," *Science*, vol. 358, pp. 745–750, Nov. 2017. Publisher: American Association for the Advancement of Science (AAAS).

[10] B. T. Diroll, G. Nedelcu, M. V. Kovalenko, and R. D. Schaller, "High-Temperature Photoluminescence of CsPbX_3 ($\text{X} = \text{Cl}, \text{Br}, \text{I}$) Nanocrystals," *Adv Funct Materials*, vol. 27, June 2017. Publisher: Wiley.

[11] S. Chen and G. Shi, "Two-Dimensional Materials for Halide Perovskite-Based Optoelectronic Devices," *Advanced Materials*, vol. 29, June 2017. Publisher: Wiley.

[12] A. Dey, J. Ye, A. De, *et al.*, "State of the Art and Prospects for Halide Perovskite Nanocrystals," *ACS Nano*, vol. 15, pp. 10775–10981, July 2021. Publisher: American Chemical Society (ACS).

[13] Y. Zhang, X. Wei, L. Gao, W. Zhao, C. Sun, J. Wei, M. Yuan, Z. Ni, J. Lu, and H. Liu, "Stable $\alpha\text{-CsPbI}_3$ with extremely red emission for expanding the color gamut," *Sci. China Inf. Sci.*, vol. 67, May 2024. Publisher: Springer Science and Business Media LLC.

[14] G. Hodes, "Perovskite-Based Solar Cells," *Science*, vol. 342, pp. 317–318, Oct. 2013. Publisher: American Association for the Advancement of Science (AAAS).

[15] G. E. Eperon, S. D. Stranks, C. Menelaou, M. B. Johnston, L. M. Herz, and H. J. Snaith, "Formamidinium lead trihalide: a broadly tunable perovskite for efficient planar heterojunction solar cells," *Energy Environ. Sci.*, vol. 7, no. 3, p. 982, 2014. Publisher: Royal Society of Chemistry (RSC).

[16] W. Nie, H. Tsai, R. Asadpour, J.-C. Blancon, A. J. Neukirch, G. Gupta, J. J. Crochet, M. Chhowalla, S. Tretiak, M. A. Alam, H.-L. Wang, and A. D. Mohite, "High-efficiency solution-processed perovskite solar cells with millimeter-scale grains," *Science*, vol. 347, pp. 522–525, Jan. 2015. Publisher: American Association for the Advancement of Science (AAAS).

[17] T. Zhang, M. I. Dar, G. Li, F. Xu, N. Guo, M. Grätzel, and Y. Zhao, "Bication lead iodide 2D perovskite component to stabilize inorganic $\alpha\text{-CsPbI}_3$ perovskite phase for high-efficiency solar cells," *Sci. Adv.*, vol. 3, Sept. 2017. Publisher: American Association for the Advancement of Science (AAAS).

[18] Y. Huang, Y. Zhang, J. Sun, X. Wang, J. Sun, Q. Chen, C. Pan, and H. Zhou, "The Exploration of Carrier Behavior in the Inverted Mixed Perovskite Single-Crystal Solar Cells," *Adv Materials Inter.*, vol. 5, July 2018. Publisher: Wiley.

[19] F. O. Saouma, C. C. Stoumpos, J. Wong, M. G. Kanatzidis, and J. I. Jang, "Selective enhancement of optical nonlinearity in two-dimensional organic-inorganic lead iodide perovskites," *Nat Commun*, vol. 8, Sept. 2017. Publisher: Springer Science and Business Media LLC.

[20] D. Wang, D. Wu, D. Dong, W. Chen, J. Hao, J. Qin, B. Xu, K. Wang, and X. Sun, "Polarized emission from CsPbX_3 perovskite quantum dots," *Nanoscale*, vol. 8, no. 22, pp. 11565–11570, 2016. Publisher: Royal Society of Chemistry (RSC).

[21] S. Pathak, N. Sakai, F. Wisnivesky Rocca Rivarola, S. D. Stranks, J. Liu, G. E. Eperon, C. Ducati, K. Wojciechowski, J. T. Griffiths, A. A. Haghhighirad, A. Pellarroque, R. H. Friend, and H. J. Snaith, "Perovskite Crystals for Tunable White Light Emission," *Chem. Mater.*, vol. 27, pp. 8066–8075, Dec. 2015. Publisher: American Chemical Society (ACS).

[22] P. Liu, W. Chen, W. Wang, B. Xu, D. Wu, J. Hao, W. Cao, F. Fang, Y. Li, Y. Zeng, R. Pan, S. Chen, W. Cao, X. W. Sun, and K. Wang, "Halide-Rich Synthesized Cesium Lead Bromide Perovskite Nanocrystals for Light-Emitting Diodes with Improved Performance," *Chem. Mater.*, vol. 29, pp. 5168–5173, June 2017. Publisher: American Chemical Society (ACS).

[23] A. Kojima, K. Teshima, Y. Shirai, and T. Miyasaka, "Organometal Halide Perovskites as Visible-Light Sensitizers for Photovoltaic Cells," *J. Am. Chem. Soc.*, vol. 131, pp. 6050–6051, May 2009.

[24] M. M. Lee, J. Teuscher, T. Miyasaka, T. N. Murakami, and H. J. Snaith, "Efficient Hybrid Solar Cells Based on Meso-Superstructured Organometal Halide Perovskites," *Science*, vol. 338, pp. 643–647, Nov. 2012.

[25] J. Burschka, N. Pellet, S.-J. Moon, R. Humphry-Baker, P. Gao, M. K. Nazeeruddin, and M. Grätzel, "Sequential deposition as a route to high-performance perovskite-sensitized solar cells," *Nature*, vol. 499, pp. 316–319, July 2013.

[26] A. Mei, X. Li, L. Liu, Z. Ku, T. Liu, Y. Rong, M. Xu, M. Hu, J. Chen, Y. Yang, M. Grätzel, and H. Han, "A hole-conductor-free, fully printable mesoscopic perovskite solar cell with high stability," *Science*, vol. 345, pp. 295–298, July 2014. Publisher: American Association for the Advancement of Science (AAAS).

[27] T. Yang, F. Li, and R. Zheng, "Recent Progress on Cesium Lead Halide Perovskites for Photodetection Applications," *ACS Appl. Electron. Mater.*, vol. 1, pp. 1348–1366, Aug. 2019.

[28] E. Kirstein, D. R. Yakovlev, M. M. Glazov, E. A. Zhukov, D. Kudlacik, I. V. Kalitukha, V. F. Sapega, G. S. Dimitriev, M. A. Semina, M. O. Nestoklon, E. L. Ivchenko, N. E. Kopteva, D. N. Dirin, O. Nazarenko, M. V. Kovalenko, A. Baumann, J. Höcker, V. Dyakonov, and M. Bayer, "The Landé factors of electrons and holes in lead halide perovskites: universal dependence on the band gap," *Nat Commun*, vol. 13, p. 3062, June 2022. Publisher: Nature Publishing Group.

[29] E. Kirstein, N. E. Kopteva, D. R. Yakovlev, E. A. Zhukov, E. V. Kolobkova, M. S. Kuznetsova, V. V. Belykh, I. A. Yugova, M. M. Glazov, M. Bayer, and A. Greilich, "Mode locking of hole spin coherences in $\text{CsPb}(\text{Cl}, \text{Br})_3$ perovskite nanocrystals," *Nat Commun*, vol. 14, p. 699, Feb. 2023. Publisher: Nature Publishing Group.

[30] M. O. Nestoklon, E. Kirstein, D. R. Yakovlev, E. A. Zhukov, M. M. Glazov, M. A. Semina, E. L. Ivchenko, E. V. Kolobkova, M. S. Kuznetsova, and M. Bayer, "Tailoring the Electron and Hole Landé Factors in Lead Halide Perovskite Nanocrystals by Quantum Confinement and Halide Exchange," *Nano Lett.*, vol. 23, pp. 8218–8224, Sept. 2023. Publisher: American Chemical Society (ACS).

[31] E. Kolobkova, M. Kuznetsova, and N. Nikonorov, "Perovskite CsPbX_3 ($\text{X}=\text{Cl}, \text{Br}, \text{I}$) Nanocrystals in fluorophosphate glasses," *Journal of Non-Crystalline Solids*, vol. 563, p. 120811, July 2021. Publisher: Elsevier BV.

[32] E. V. Kulebyakina, "Temperature-dependent photoluminescence dynamics of CsPbBr_3 and $\text{CsPb}(\text{Cl}, \text{Br})_3$ perovskite nanocrystals in a glass matrix," *Phys. Rev. B*, vol. 109, no. 23, 2024.

- [33] U. Ekenberg, “Nonparabolicity effects in a quantum well: Sublevel shift, parallel mass, and Landau levels,” *Phys. Rev. B*, vol. 40, pp. 7714–7726, Oct. 1989. Publisher: American Physical Society (APS).
- [34] S. Tomić, E. P. O'Reilly, P. J. Klar, H. Grüning, W. Heimbrot, W. M. Chen, and I. A. Buyanova, “Influence of conduction-band nonparabolicity on electron confinement and effective mass in $\text{GaN}_x\text{As}_{1-x}/\text{GaAs}$ quantum wells,” *Phys. Rev. B*, vol. 69, June 2004. Publisher: American Physical Society (APS).
- [35] L. D. Whalley, J. M. Frost, B. J. Morgan, and A. Walsh, “Impact of nonparabolic electronic band structure on the optical and transport properties of photovoltaic materials,” *Phys. Rev. B*, vol. 99, p. 085207, Feb 2019.
- [36] M. Nestoklon, “Tight-binding description of inorganic lead halide perovskites in cubic phase,” *Computational Materials Science*, vol. 196, p. 110535, Aug. 2021. Publisher: Elsevier BV.
- [37] S. J. Clark, M. D. Segall, C. J. Pickard, P. J. Hasnip, M. I. J. Probert, K. Refson, and M. C. Payne, “First principles methods using CASTEP,” *Zeitschrift für Kristallographie - Crystalline Materials*, vol. 220, pp. 567–570, May 2005. Publisher: Walter de Gruyter GmbH.
- [38] A. Tkatchenko and M. Scheffler, “Accurate Molecular Van Der Waals Interactions from Ground-State Electron Density and Free-Atom Reference Data,” *Physical Review Letters*, vol. 102, Feb. 2009. Publisher: American Physical Society (APS).
- [39] K. Refson, P. R. Tulip, and S. J. Clark, “Variational density-functional perturbation theory for dielectrics and lattice dynamics,” *Physical Review B*, vol. 73, Apr. 2006. Publisher: American Physical Society (APS).
- [40] J. Aarons, “A New CASTEP and ONETEP Geometry Optimiser.,” 2011.
- [41] R. H. Byrd, J. Nocedal, and R. B. Schnabel, “Representations of quasi-Newton matrices and their use in limited memory methods,” *Math. Program.*, vol. 63, pp. 129–156, Jan. 1994.
- [42] R. Sutton *et al.*, “Cubic or orthorhombic? revealing the crystal structure of metastable black-phase CsPbI_3 by theory and experiment,” *Univ. of Oxford (preprint) / published work*, 2018. GW and LDA calculations, Table 2 reports effective masses for $\gamma\text{-CsPbI}_3$.
- [43] A. Jain, S. P. Ong, G. Hautier, W. Chen, W. D. Richards, S. Dacek, S. Cholia, D. Gunter, D. Skinner, G. Ceder, and K. A. Persson, “Commentary: The Materials Project: A materials genome approach to accelerating materials innovation,” *APL Materials*, vol. 1, p. 011002, July 2013.
- [44] M. K. Horton, P. Huck, R. X. Yang, J. M. Munro, S. Dwaraknath, A. M. Ganose, R. S. Kingsbury, M. Wen, J. X. Shen, T. S. Mathis, A. D. Kaplan, K. Berket, J. Riebesell, J. George, A. S. Rosen, E. W. C. Spotte-Smith, M. J. McDermott, O. A. Cohen, A. Dunn, M. C. Kuner, G.-M. Rignanese, G. Petretto, D. Waroquiers, S. M. Griffin, J. B. Neaton, D. C. Chrzan, M. Asta, G. Hautier, S. Cholia, G. Ceder, S. P. Ong, A. Jain, and K. A. Persson, “Accelerated data-driven materials science with the Materials Project,” *Nat. Mater.*, vol. 24, pp. 1522–1532, Oct. 2025.
- [45] H. J. Monkhorst and J. D. Pack, “Special points for Brillouin-zone integrations,” *Physical Review B*, vol. 13, pp. 5188–5192, June 1976. Publisher: American Physical Society (APS).
- [46] P. Y. Yu and M. Cardona, *Fundamentals of Semiconductors: Physics and Materials Properties*. Graduate Texts in Physics, Berlin, Heidelberg: Springer Berlin Heidelberg, 2010.
- [47] E. O. Kane, “Band structure of indium antimonide,” *Journal of Physics and Chemistry of Solids*, vol. 1, pp. 249–261, 1957. originally published 1957.
- [48] M. Altarelli and N. O. Lipari, “Exciton dispersion in semiconductors with degenerate bands,” *Physical Review B*, vol. 15, pp. 4898–4906, 1977.
- [49] D. K. Loginov, “Exact numeric calculation of nonparabolicity of exciton dispersion in semiconductors with degenerate valence band,” *Physica B: Condensed Matter*, vol. 715, p. 417534, 2025.
- [50] E. M. Lifshitz, *Quantum Electrodynamics*. Elsevier Butterworth-Heinemann, 1982.